TRIM14 inhibits OPTN-mediated autophagic degradation of KDM4D to epigenetically regulate inflammation

Di Liu[a,1], Zhiyao Zhao[a,b,1], Yuanchu She[a,1], Lei Zhang[a], Xiangtian Chen[a], Ling Ma[a], and Jun Cui[a,2]

[a]Guangdong Province Key Laboratory of Pharmaceutical Functional Genes, MOE Key Laboratory of Gene Function and Regulation, State Key Laboratory of Biocontrol, School of Life Sciences, Sun Yat-sen University, Guangdong 510275, People's Republic of China; and [b]Department of Internal Medicine, Guangzhou Institute of Pediatrics, Guangzhou Women and Children's Medical Center, Guangdong 510623, People's Republic of China

Edited by Noboru Mizushima, Department of Biochemistry and Molecular Biology, University of Tokyo, Graduate School and Faculty of Medicine, Tokyo, Japan; received July 21, 2021; accepted January 5, 2022 by Editorial Board Member Tadatsugu Taniguchi

Autophagy is a fundamental cellular process of protein degradation and recycling that regulates immune signaling pathways via multiple mechanisms. However, it remains unclear how autophagy epigenetically regulates the immune response. Here, we identified TRIM14 as an epigenetic regulator that reduces histone H3K9 trimethylation by inhibiting the autophagic degradation of the histone demethylase KDM4D. TRIM14 recruited the deubiquitinases USP14 and BRCC3 to cleave the K63-linked ubiquitin chains of KDM4D, which prevented KDM4D from undergoing optineurin (OPTN)-mediated selective autophagy. Tripartite motif-containing 14 (TRIM14) deficiency in dendritic cells significantly impaired the expression of the KDM4D-directed proinflammatory cytokines interleukin 12 (*Il12*) and *Il23* and protected mice from autoimmune inflammation. Taken together, these findings highlight the cross-talk between epigenetic regulation and autophagy and suggest TRIM14 is a potential target of therapeutic intervention for inflammation-related diseases.

inflammation | autophagy | epigenetic regulation | TRIM14 | KDM4D

Accumulating evidence has suggested that autophagy, a highly conserved eukaryotic degradation process, is deeply involved in the regulation of immune responses, including the elimination of pathogens, production of inflammatory cytokines and type I interferons (IFNs), presentation of antigens, development of lymphocytes, and immune evasion of cancer (1–4). Autophagy-mediated protein degradation can be highly selective and relies on a number of cargo receptors to recognize the diverse substrates and deliver them to autolysosomes by interacting with lipidized ATG8 family proteins (5). Many cargo receptors—including p62/SQSTM1, NBR1, NDP52/CALCOCO2, TAX1BP1, optineurin (OPTN), and Tollip—can recognize polyubiquitin chains on substrates as autophagic degradation signals (6). Ubiquitination is an important posttranscriptional modification that is reversibly controlled by multiple ubiquitin ligases and deubiquitinases (DUBs) (7). Tripartite motif-containing (TRIM) proteins, an essential family of E3 ubiquitin ligases, have been reported to extensively participate in the regulation of innate immune signaling as well as autophagy (8). We previously demonstrated that TRIM14 positively regulates type I IFN signaling and noncanonical NF-κB signaling by modulating selective autophagy, indicating that TRIM proteins might play a critical role in orchestrating the cross-talk between autophagy and innate immunity at the cell signaling level (9, 10). However, the autophagic control of innate immune responses at the epigenetic level remains largely unclear.

Various studies have shown that histone methylation plays a central role in regulating immune responses and inflammation at the epigenetic level (11–15). The histone methyltransferase Wbp7 facilitates *Pigp* transcription by increasing histone H3 lysine 4 trimethylation (H3K4me3) modification at its promoter to promote the glycosylphosphatidylinositol anchor-mediated membrane binding of CD14 to primary macrophages (16). Lysine demethylase 5A (KDM5A) removes H3K4me3 modification at the *Socs1* promoter to inhibit the expression of suppressor of cytokine signaling 1 (SOCS1), leading to signal transducer and activator of transcription 4 (STAT4) activation and IFN-γ production in natural killer cells, as well as to resistance to *Listeria monocytogenes* infection in mice (17). G9a enhances H3K9me2 at promoters of IFN and IFN-stimulated genes to inhibit their production in fibroblasts and dendritic cells (DCs) (18). Histone demethylase KDM4D (also known as JMJD2D) removes H3K9me3 around *Mdc* and interleukin 12b (*Il12b*) enhancers to strictly regulate their expression in DCs and macrophages (19). Interestingly, it has been reported that the DUB Trabid specifically promotes *Il12*- and *Il23*-mediated inflammation by preventing KDM4D from undergoing proteasome-dependent protein degradation (20). We also showed that USP38 specifically inhibited proteasomal degradation of KDM5B to resolve inflammation, further indicating the importance of histone methylases and demethylases in immune regulation (11).

Significance

Histone methylation regulates gene transcription through a variety of methylases and demethylases. The regulatory role of autophagy, an important process of protein degradation and recycling, in these histone modifiers is still unclear. We report that TRIM14 stabilized the histone demethylase KDM4D to facilitate the transcription of interleukin 12 (*Il12*) and *Il23* by inhibiting histone H3K9 trimethylation in vitro and in vivo. Mechanistically, TRIM14 recruited the deubiquitinases USP14 and BRCC3 to remove the K63-linked ubiquitin chains of KDM4D and prevented it from undergoing optineurin-mediated autophagic degradation. This study is valuable not only for increasing our understanding of the cross-talk between autophagy and epigenetic regulation, but also for demonstrating the potential of TRIM14 as a target for therapeutic interventions for inflammation-related diseases.

Author contributions: D.L., Z.Z., Y.S., and J.C. designed research; D.L., Z.Z., Y.S., and L.Z. performed research; D.L., Z.Z., Y.S., X.C., and L.M. analyzed data; and D.L., Z.Z., Y.S., X.C., L.M., and J.C. wrote the paper.

The authors declare no competing interest.

This article is a PNAS Direct Submission. N.M. is a guest editor invited by the Editorial Board.

[1]D.L., Z.Z., and Y.S. contributed equally to this work.

[2]To whom correspondence may be addressed. Email: cuij5@mail.sysu.edu.cn.

This article contains supporting information online at http://www.pnas.org/lookup/suppl/doi:10.1073/pnas.2113454119/-/DCSupplemental.

Published February 10, 2022.

Here, we demonstrated an autophagy-dependent regulatory mechanism in which TRIM14 reduced histone H3K9 trimethylation (H3K9me3) to promote *Il12*- and *Il23*-mediated inflammatory responses at the epigenetic level. Mechanistically, TRIM14 recruited USP14 and BRCC3 to remove the K63-linked ubiquitination of KDM4D and prevented it from undergoing OPTN-mediated selective autophagic degradation. TRIM14 deficiency in mice causes reduced inflammatory responses in an experimental autoimmune encephalomyelitis (EAE) model. These results highlight an epigenetically dependent regulatory mechanism in which TRIM14 couples autophagy and histone methylation to selectively modulate proinflammatory cytokine production to promote inflammation.

Results

TRIM14 Negatively Regulates H3K9me2 and H3K9me3 by Stabilizing KDM4D. To investigate the potential epigenetic regulation functions of TRIM14, we examined alternations of several histone modifications in Flag-TRIM14–inducible HeLa cells. We found that TRIM14 negatively regulated H3K9me2 and H3K9me3 (Fig. 1*A*), but not other histone modifications, such as H3K4me3, H2A ubiquitination (H2Aub), or H2Bub (*SI Appendix*, Fig. S1*A*). *Trim14*$^{-/-}$ bone marrow-derived DCs (BMDCs) consistently showed increased levels of H3K9me2 and H3K9me3 (Fig. 1*B*) but not H3K4me3, H2Aub, or H2Bub compared with WT cells (*SI Appendix*, Fig. S1*B*). Immunofluorescence analysis showed that overexpression of TRIM14 led to a reduction in H3K9me3 levels compared with those in untransfected cells (Fig. 1*C*). Collectively, these data suggest that TRIM14 negatively regulates H3K9me3.

Since TRIM14 is not a histone demethylase, we next investigated whether TRIM14 affects H3K9me3 by modulating the protein stability of specific H3K9 demethylases. With ectopic expression of TRIM14, the protein levels of H3K9 demethylase KDM4D increased (*SI Appendix*, Fig. S1*C*), while there was no difference in other H3K9 demethylases, such as KDM3B (*SI Appendix*, Fig. S1*D*), KDM4A (*SI Appendix*, Fig. S1*E*), and KDM4B (*SI Appendix*, Fig. S1*F*). In addition, the KDM4D protein levels positively correlated with TRIM14 expression (Fig. 2*A* and *SI Appendix*, Fig. S2*A*), while the H3K9me3 levels showed the opposite pattern (*SI Appendix*, Fig. S2*B*). However, the mRNA levels of *KDM4D* did not change with overexpression of TRIM14 (Fig. 2*A*). Consistent with these results, we further confirmed that knockout of *TRIM14* markedly decreased KDM4D protein levels and promoted H3K9me3 (Fig. 2*B*). To investigate whether TRIM14 affected H3K9me3 through

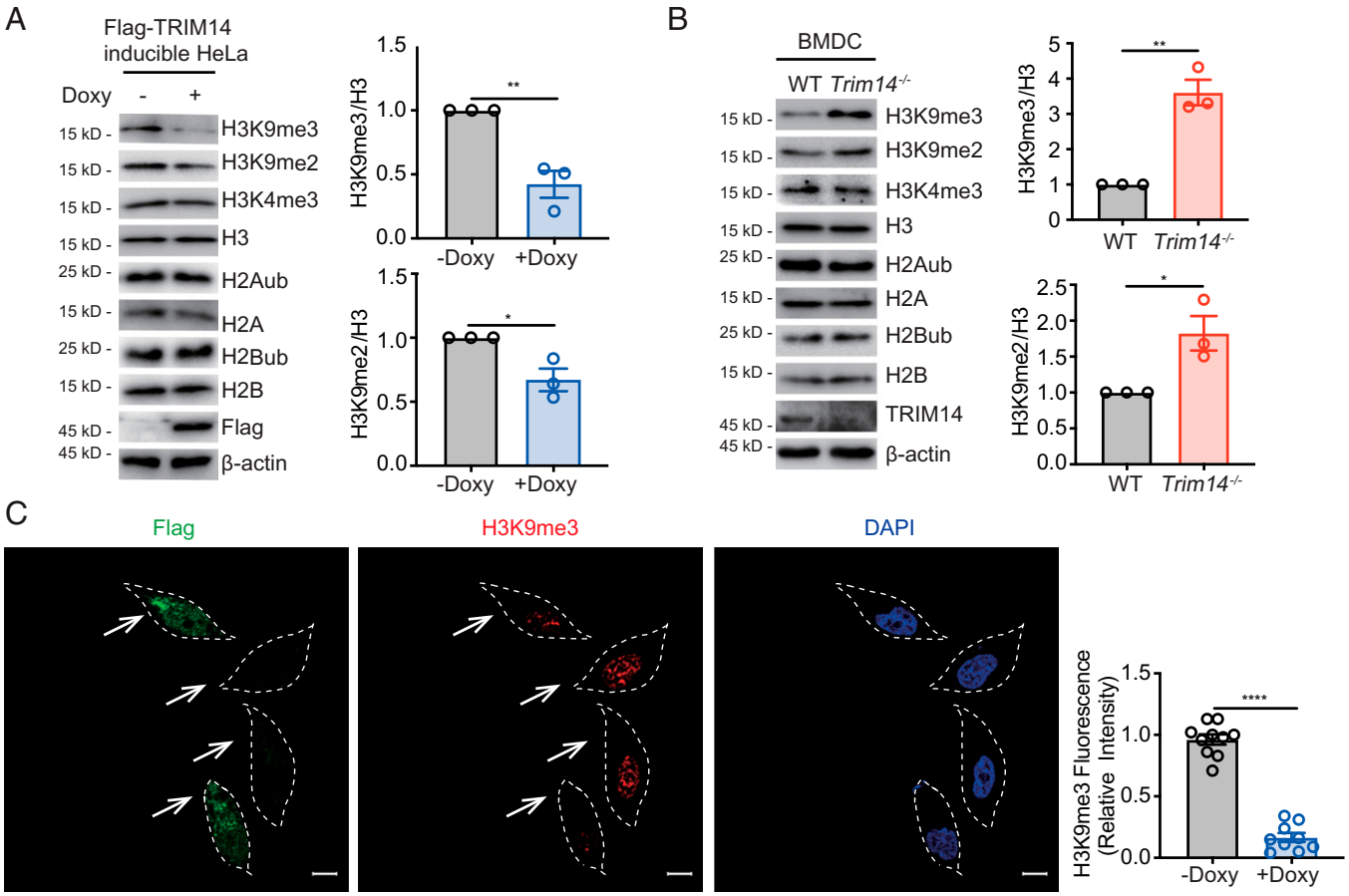

Fig. 1. TRIM14 negatively regulates H3K9me2 and H3K9me3. (*A*) Flag-TRIM14–inducible HeLa cells were treated with 200 ng/mL Doxy for 12 h, and cell extracts were collected for immunoblot analysis of H3K9me3, H3K9me2, H3K4me3, H2Aub, and H2Bub. The protein levels of H3K9me3/H3 and H3K9me2/H3 were quantified by ImageJ software (NIH). (*B*) Cell extracts of WT or *Trim14*$^{-/-}$ BMDCs were harvested for immunoblot analysis of these histone modifications. The protein levels of H3K9me3/H3 and H3K9me2/H3 were analyzed by ImageJ software (NIH). (*C*) Flag-TRIM14–inducible HeLa cells were treated with 200 ng/mL Doxy for 12 h, and then the cells were stained with anti-Flag (green) and anti-H3K9me3 (red) antibodies to detect TRIM14 and H3K9me3 levels via confocal microscopy. The relative intensity of H3K9me3 fluorescence signals (red) in TRIM14-overexpressing cells (green) versus control cells (no signal) in the same image was analyzed by ImageJ software (NIH). (Scale bars, 100 μm.) In *A* and *B*, data are shown as mean values ± SEM, with unpaired two-tailed Student's *t* test (three independent experiments). In *C*, the data show the mean values ± SEM, with unpaired two-tailed Student's *t* test (n = ~50 cells), $^{*}P < 0.05$, $^{**}P < 0.01$, $^{****}P < 0.0001$.

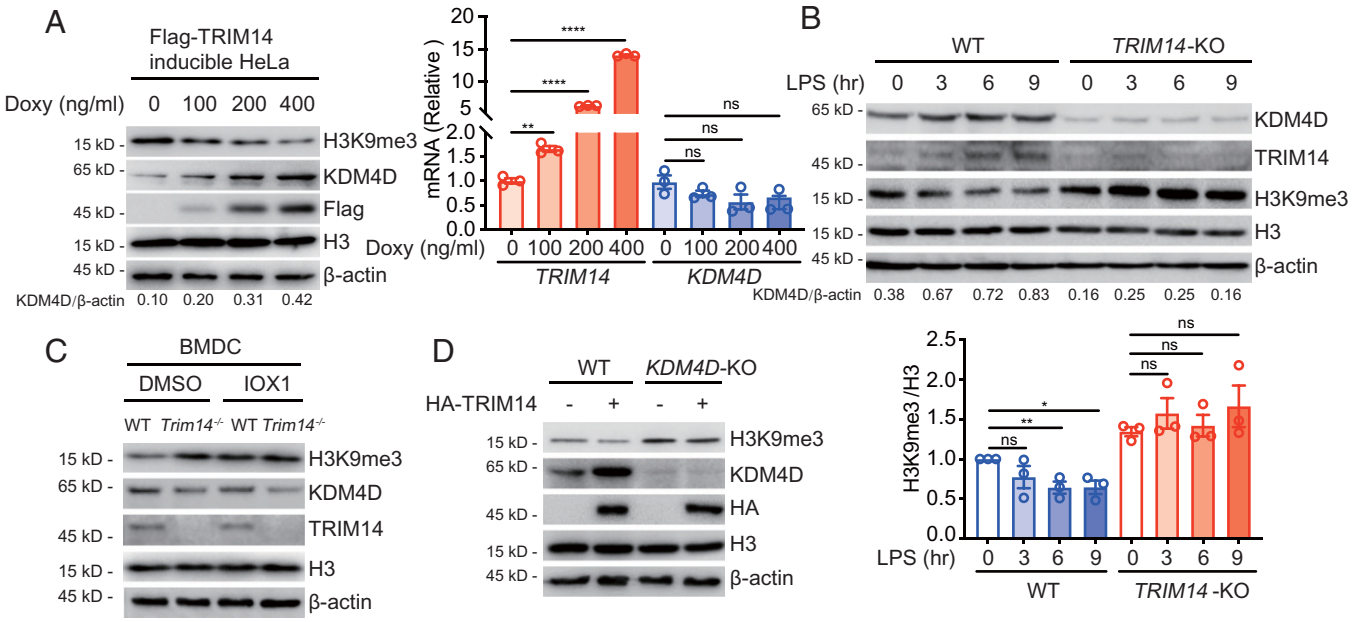

Fig. 2. TRIM14 reduces H3K9me3 through stabilizing KDM4D. (*A*) Flag-TRIM14–inducible HeLa cells were treated with the indicated concentration of Doxy for 12 h. Then, the cells were harvested for immunoblot analysis of H3K9me3 and KDM4D levels or to quantify the mRNA levels of *TRIM14* and *KDM4D*. ImageJ software (NIH) was used to quantify the protein levels of KDM4D/β-actin. (*B*) Immunoblot analysis of KDM4D, H3K9me3 and TRIM14 in WT or *TRIM14*-KO HeLa cells treated with 100 ng/mL LPS, as indicated. The protein levels of KDM4D/β-actin and H3K9me3/H3 were analyzed by ImageJ software (NIH). (*C*) Immunoblot analysis of H3K9me3 and KDM4D in WT or *Trim14*$^{-/-}$ BMDCs treated with DMSO or IOX1 (50 μM, 3 h). (*D*) Immunoblot analysis of H3K9me3 levels in extracts of WT or *KDM4D*-KO HEK293T cells, with or without overexpressed HA-TRIM14. In *A* and *B*, data are mean values ± SEM and *P* values were calculated by unpaired two-tailed Student's *t* test (three independent experiments). ns, not significant, **P* < 0.05, ***P* < 0.01, *****P* < 0.0001.

KDM4D, we blocked the activity of KDM4D with IOX1, a broad-spectrum inhibitor of histone demethylases, and found that TRIM14 deficiency no longer resulted in an up-regulation of H3K9me3 (Fig. 2*C* and *SI Appendix*, Fig. S2*C*). Moreover, the reduction in H3K9me3 caused by ectopic expression of TRIM14 was abolished by KDM4D deficiency (Fig. 2*D* and *SI Appendix*, Fig. S2*D*). These results suggest that TRIM14 negatively regulates H3K9me3 by up-regulating the protein levels of KDM4D.

TRIM14 Interacts with KDM4D to Inhibit Its Autophagic Degradation. To discover the underlying mechanisms of how TRIM14 stabilizes KDM4D, we examined the interaction between TRIM14 and KDM4D. TRIM14 interacted with KDM4D under physiological conditions, and this interaction increased as TRIM14 abundance increased upon lipopolysaccharide (LPS) treatment in BMDCs (Fig. 3*A* and *SI Appendix*, Fig. S2*E*). Confocal microscopy analysis showed that TRIM14 and KDM4D colocalization was elevated after tumor necrosis factor-α (TNF-α) treatment (Fig. 3*B*). Since the overall expression of TRIM14 also appeared to increase with TNF-α treatment, we transfected plasmids encoding HA-TRIM14 into HeLa cells to detect interactions between KDM4D and HA-TRIM14. We observed no difference in HA-TRIM14–KDM4D interactions with LPS stimulation, indicating that LPS does not directly affect the interaction of TRIM14 and KDM4D (*SI Appendix*, Fig. S2*F*).

We next determined which degradation pathway of KDM4D was blocked by TRIM14 and found that the autophagy-sequestration inhibitor 3-methyladenine (3MA) reduced the effect of TRIM14 overexpression on KDM4D levels (Fig. 3*C*). Moreover, Earle's balanced salt solution (EBSS) induced autophagic degradation of KDM4D, which could be rescued by TRIM14 overexpression (*SI Appendix*, Fig. S3*A*). Consistent with these findings, TRIM14 failed to stabilize KDM4D in *ATG5* knockout (KO) (Fig. 3*D* and *SI Appendix*, Fig. S3*B*) or *BECN1*-KO (*SI Appendix*, Fig. S3*C*) HEK293T cells, in which autophagy is severely attenuated. Therefore, TRIM14 plays a role in controlling KDM4D stability via the autolysosome pathway. Microtubule-associated protein 1A/1B-light chain 3 (LC3) is considered a marker of autophagosomes and reflects the autophagy process (21). As Sparrer et al. showed a modest effect of TRIM14 overexpression on the induction of GFP-LC3 puncta formation (22), we overexpressed different concentrations of plasmids encoding HA-TRIM14 in HeLa cells and found that the protein levels of LC3 II, a conjugated form of LC3, were dependent on the dose of exogeneous TRIM14 (*SI Appendix*, Fig. S3*D*). In our experimental system, modest TRIM14 overexpression did not affect global autophagy (*SI Appendix*, Fig. S3 *E* and *F*). We further demonstrated that TRIM14 overexpression blocked the interaction of KDM4D and LC3 both in a coimmunoprecipitation (co-IP) assay (Fig. 3*E* and *SI Appendix*, Fig. S3*G*) and in immunofluorescence analysis (*SI Appendix*, Fig. S3*H*). Collectively, our data demonstrate that TRIM14 suppresses the autophagic degradation of KDM4D.

TRIM14 Inhibits OPTN-Mediated Selective Autophagic Degradation of KDM4D. Autophagy can be highly selective, with the specificity of substrate recognition by selective autophagy dependent on cargo receptors (6). To identify which cargo receptor is involved in the autophagic degradation of KDM4D, we examined the interaction of KDM4D and several known cargo receptors and found that KDM4D interacted with p62, OPTN, and NDP52 in the overexpression system (Fig. 4*A*). To confirm that whether these receptors mediated KDM4D stability, we constructed *SQSTM1*- (a gene encoding p62), *CALCOCO2*- (a gene encoding NDP52), and *OPTN*-KO cell lines and found that only the *OPTN*-KO, but not of the *SQSTM1*- or *CALCOCO2*-KO, led to increased protein levels of KDM4D. TRIM14 overexpression was unable to further stabilize KDM4D in the absence of OPTN (*SI Appendix*, Fig. S4 *A* and *B*).

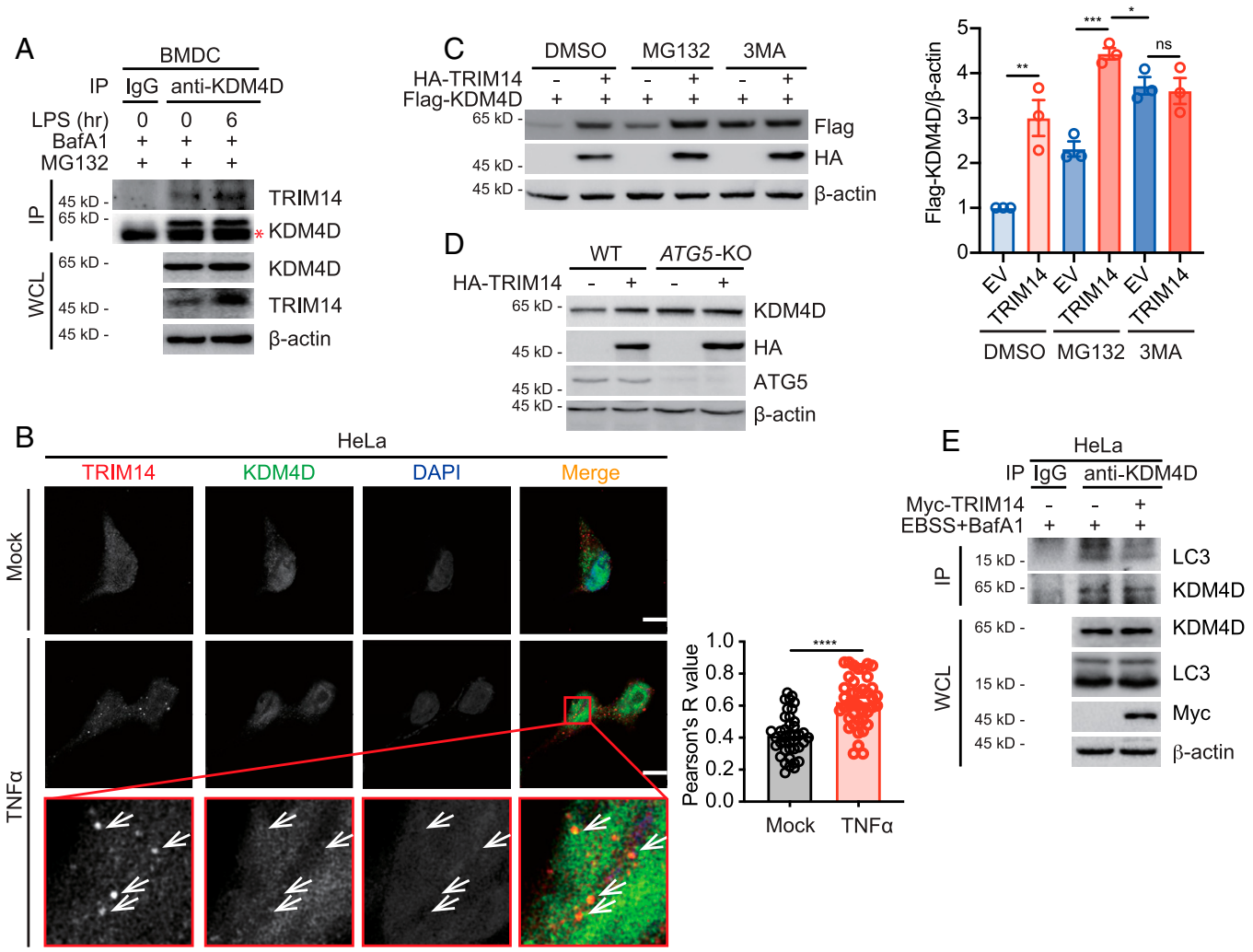

Fig. 3. TRIM14 interacts with KDM4D to inhibit its autophagic degradation. (*A*) BMDCs were treated with 100 ng/mL LPS, 0.3 μM BafA1, and 5 μM MG132, and cell extracts were collected for co-IP and immunoblot analysis of the interaction of TRIM14 and KDM4D. The red asterisk indicates the band of heavy chains. WCL, whole-cell lysates. (*B*) HeLa cells were treated with 50 ng/mL TNF-α for 6 h, and then the cells were stained with anti-TRIM14 (red) and anti-KDM4D (green) antibodies, as well as DAPI (blue) to detect the colocalization of TRIM14 and KDM4D by confocal microscopy. (Scale bar, 10 μm.) Statistics shown refer to the correlation between TRIM14 and KDM4D in the indicated samples. (*C*) Immunoblot analysis of KDM4D stabilization in HEK293T cells transfected with Flag-KDM4D or HA-TRIM14, followed by DMSO, MG132 (5 μM), or 3MA (5 mM) treatment for 6 h. The protein levels of Flag-KDM4D/β-actin were quantified by ImageJ software (NIH). (*D*) Immunoblot analysis of KDM4D in WT or *ATG5*-KO HEK293T cells transfected with HA-TRIM14. (*E*) HeLa cells were transfected with Myc-TRIM14 and treated with EBSS for 3 h and 0.3 μM BafA1 for 6 h. Then, the cell extracts were harvested for co-IP and immunoblot analysis of the interaction of KDM4D and LC3 II. In *B*, the data show the mean values ± SEM, and *P* values were determined by unpaired two-tailed Student's *t* tests (n = ~50 cells). In *C*, data are mean values ± SEM and *P* values were calculated by unpaired two-tailed Student's *t* tests (three independent experiments). ns, not significant, $*P < 0.05$, $**P < 0.01$, $***P < 0.001$, $****P < 0.0001$.

Knockdown of *TRIM14* did not influence the protein levels of endogenous KDM4D in *OPTN*-KO cells (Fig. 4*B* and *SI Appendix*, Fig. S4*C*). We further showed that KDM4D interacted with OPTN in BMDCs through co-IP assays and mass spectrometry (MS) analysis (Fig. 4 *C* and *D* and *SI Appendix*, Fig. S4*D*). We found that the interaction of KDM4D and OPTN was inhibited by TRIM14 (Fig. 4*E*). Confocal analysis also showed reduced colocalization puncta of KDM4D–OPTN upon TRIM14 overexpression (*SI Appendix*, Fig. S4*E*).

Consistent with these findings, interaction of KDM4D and OPTN was increased in *TRIM14*-KO cells compared with WT cells (Fig. 4*F* and *SI Appendix*, Fig. S4*F*). As KDM4D functions as a demethylase of H3K9me2 and H3K9me3, we stimulated WT and *OPTN*-KO HEK293T cells with TNF-α to induce inflammation and investigated the dynamic changes in H3K9me2 and H3K9me3. We found that TNF-α treatment decreased the levels of H3K9me2 and H3K9me3 in WT cells. In addition, the abundance of H3K9me3 in *OPTN*-KO cells with TNF-α stimulation was further attenuated than that in WT cells (Fig. 4*G*). Next, we detected the protein levels of OPTN and KDM4D in WT and *TRIM14*-KO HeLa cells and found that KDM4D, but not OPTN, was obviously decreased in *TRIM14*-KO cells compared with WT cells (*SI Appendix*, Fig. S4*G*). In addition, TRIM14 overexpression did not affect the interaction of OPTN and LC3 II (*SI Appendix*, Fig. S4*H*). Although we observed that TRIM14 interacted with OPTN in HeLa cells (*SI Appendix*, Fig. S4*I*), further experiments showed that the KDM4D–TRIM14 interaction was not dependent on OPTN (*SI Appendix*, Fig. S4*J*). Taken together, these results indicate that TRIM14 inhibits OPTN-mediated selective autophagic degradation of KDM4D by blocking the KDM4D–OPTN interaction.

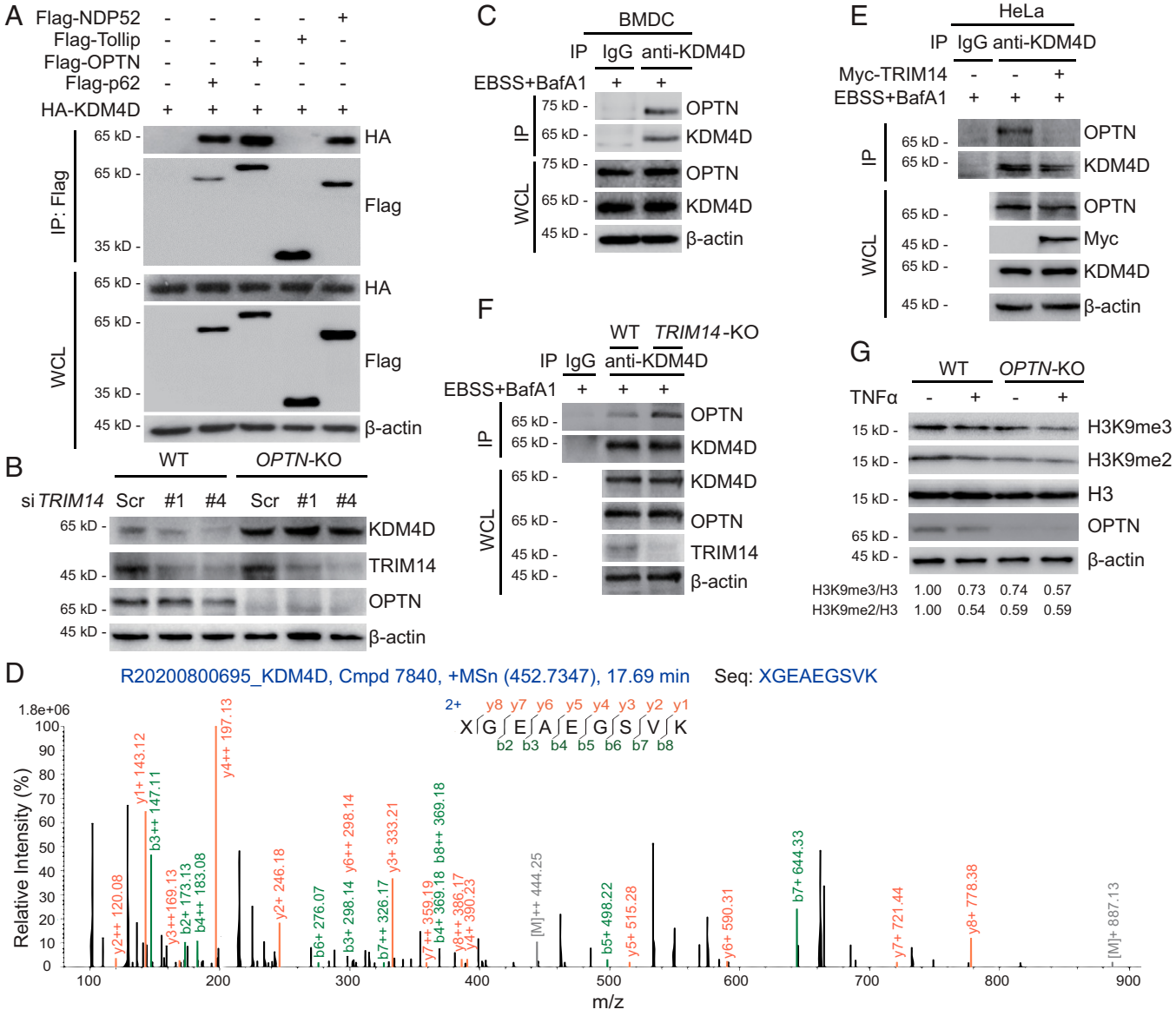

Fig. 4. TRIM14 inhibits OPTN-mediated selective autophagic degradation of KDM4D. (*A*) Co-IP and immunoblot analysis of the interaction of KDM4D and cargo receptors in extracts of HEK293T cells transfected with HA-KDM4D, Flag-NDP52, Flag-Tollip, Flag-OPTN, or Flag-p62. (*B*) Immunoblot analysis of WT and *OPTN*-KO HEK293T cells transfected with *TRIM14* siRNAs (#1, #4) or scrambled siRNA (Scr). (*C*) Co-IP and immunoblot analysis of the interaction of KDM4D and OPTN in BMDCs treated with EBSS (3 h) and BafA1 (0.3 μM, 6 h). (*D*) MS analysis of proteins that interacted with KDM4D, including the OPTN peptide. (*E*) HeLa cells were transfected with Myc-TRIM14 and treated with EBSS (3 h) and BafA1 (0.3 μM, 6 h). Then, cell extracts were harvested for co-IP and immunoblot analysis to detect the interaction of KDM4D and OPTN. (*F*) Co-IP and immunoblot analysis of the interaction of KDM4D and OPTN in WT and *TRIM14*-KO HEK293T cells. (*G*) Immunoblot analysis of H3K9me3 and H3K9me2 levels in WT and *OPTN*-KO HEK293T cells stimulated with or without TNF-α (50 ng/mL, 6 h). H3K9me3/H3 and H3K9me2/H3 were quantified with ImageJ software (NIH). In *A*–*C* and *E*–*G*, all the experiments were repeated three times with similar results.

TRIM14 Recruits USP14 and BRCC3 to Remove the K63-Linked Ubiquitination of KDM4D. Ubiquitin chains serve as a major signal for cargo receptor recognition (23). To investigate whether OPTN-mediated degradation of KDM4D depends on the ubiquitin chains attached to it, we constructed plasmids encoding OPTN mutants deficient in the ubiquitination-binding domain (OPTN-ΔUBD) and found that the interaction of KDM4D and OPTN-ΔUBD was significantly decreased (*SI Appendix*, Fig. S5*A*). Since the ubiquitination of KDM4D was involved in its degradation, we hypothesized that TRIM14 inhibited the interaction of KDM4D and OPTN by affecting its ubiquitination state. Indeed, TRIM14 overexpression significantly decreased the ubiquitination of KDM4D (Fig. 5*A*). As the type of polyubiquitination has been shown to determine protein fate (7), we set out to analyze which type of KDM4D ubiquitination was inhibited by TRIM14. Our results showed that K63-linked ubiquitination of KDM4D was significantly decreased by TRIM14 overexpression (*SI Appendix*, Fig. S5*B*). The level of K63-linked ubiquitination of KDM4D was consistently elevated in *Trim14*$^{-/-}$ BMDCs compared with that in WT BMDCs (Fig. 5*B*). We next found that knockdown of ubiquitin-conjugating enzyme 2N (UBE2N, a K63-specific ubiquitin conjugase) (24, 25) decreased not only the K63-linked ubiquitination of KDM4D but also the interaction of KDM4D and OPTN (*SI Appendix*, Fig. S5*C*). Additionally, we constructed several plasmids encoding mutants of KDM4D, which had a

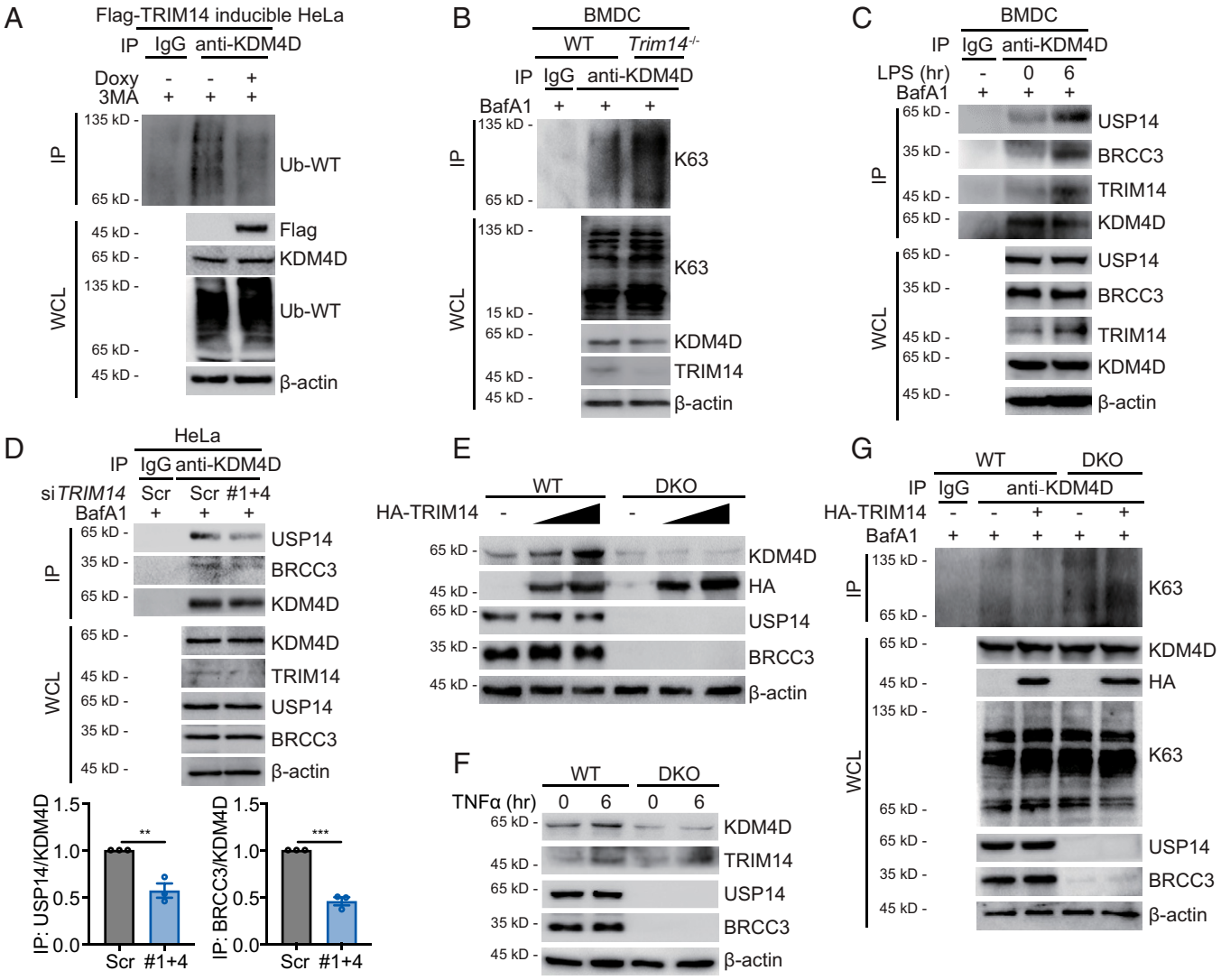

Fig. 5. TRIM14 recruits USP14 and BRCC3 to deubiquitinate KDM4D. (*A*) Co-IP and immunoblot analysis demonstrate decreased ubiquitination of KDM4D in Flag-TRIM14 inducible HeLa cells treated with Doxy (200 ng/mL) in the presence of 3MA (5 mM). (*B*) WT or *Trim14*$^{-/-}$ BMDCs were treated with 0.3 μM BafA1 for 6 h, and then cell extracts were collected for co-IP and immunoblot analysis of K63-linked ubiquitination of KDM4D. (*C*) Co-IP and immunoblot analysis of the interaction of KDM4D and TRIM14, USP14, or BRCC3 in BMDCs with or without LPS (100 ng/mL) treatment. (*D*) HeLa cells were transfected with si*TRIM14* (#1 + 4) or scrambled siRNA (Scr), and treated with BafA1 (0.3 μM, 6 h). Then, cell extracts were collected for co-IP and immunoblot analysis of the interaction of KDM4D and USP14 or BRCC3. Quantifications of IP: USP14/KDM4D and IP: BRCC3/KDM4D were performed in ImageJ software (NIH). $^{**}P < 0.01$, $^{***}P < 0.001$. (*E* and *F*) Immunoblot analysis of KDM4D levels in WT or *USP14*/*BRCC3* DKO HEK293T cells transfected with increasing doses of HA-TRIM14 (*E*) or treated with TNF-α (50 ng/mL) for the indicated times (*F*). (*G*) Co-IP and immunoblot analysis of K63-linked ubiquitination of KDM4D in WT or DKO HEK293T cells transfected with HA-TRIM14 and treated with BafA1 (0.3 μM, 6 h). In *A*–*G*, all of the experiments were repeated three times with similar results.

single K-to-R substitution at potential ubiquitination sites that were predicted in silico (http://bdmpub.biocuckoo.org/), and found that the KDM4D K472R mutant was no longer stabilized by TRIM14 (*SI Appendix*, Fig. S5*D*). Furthermore, co-IP assays and immunoassays showed that the K63-linked ubiquitination of the KDM4D K472R mutant was markedly lower than that of WT KDM4D (*SI Appendix*, Fig. S5*E*), suggesting that the ubiquitination of KDM4D is critical for OPTN recognition as well as its degradation.

Since TRIM14 is not a DUB, we hypothesized that TRIM14 might function as a platform to recruit other DUBs to remove the ubiquitin chains on KDM4D (9). Previously, we identified two TRIM14-associated DUBs, USP14 and BRCC3, from MS analysis and showed that TRIM14 specifically recruited USP14 to remove different types of ubiquitin chains attached to cGAS or p100/p52 (9, 10). In the present study, we observed that both USP14 and BRCC3 were recruited to KDM4D in BMDCs upon LPS stimulation (Fig. 5*C*). Moreover, the interaction of KDM4D and USP14/BRCC3 was increased with TRIM14 overexpression (*SI Appendix*, Fig. S5*F*), while TRIM14 deficiency significantly abrogated this interaction (Fig. 5*D*). Interestingly, we found that TRIM14 still stabilized KDM4D in *USP14*-KO (*SI Appendix*, Fig. S5*G*) and *BRCC3*-KO (*SI Appendix*, Fig. S5*H*) cells. Thus, we constructed *USP14*/*BRCC3* double KO (DKO) cells to examine whether these two DUBs were both necessary to mediate the deubiquitination and stabilization of KDM4D. We found that TRIM14 no longer influenced the protein levels of KDM4D in *USP14*/*BRCC3*-DKO HEK293T cells (Fig. 5*E* and *SI Appendix*, Fig. S5*I*). Consistent with this finding, there was no difference in the abundance of KDM4D in

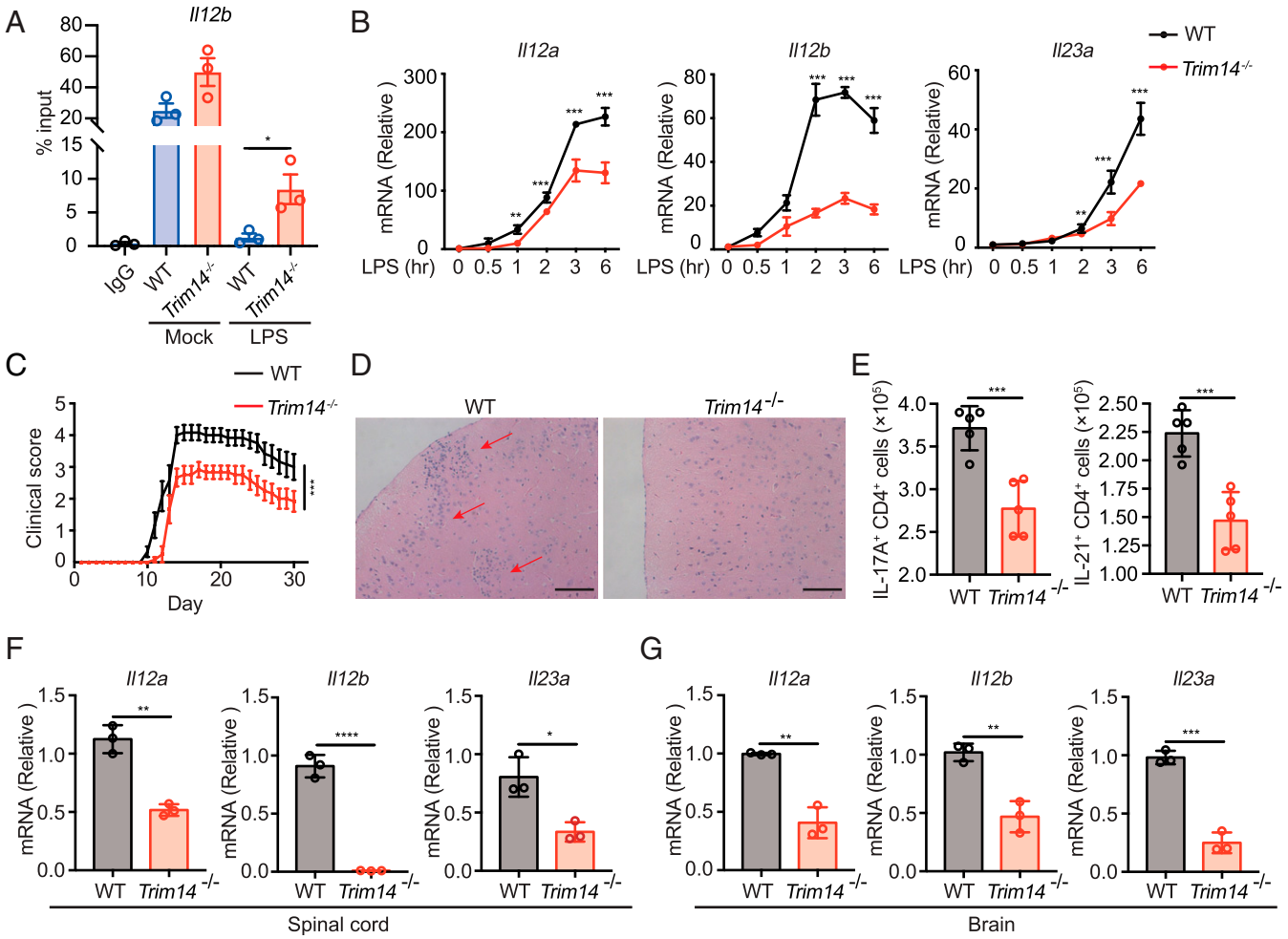

Fig. 6. TRIM14-deficient mice are resistant to EAE. (*A*) ChIP assays of H3K9me3 modification at the promoter of *Il12b* in WT or *Trim14*$^{-/-}$ BMDCs with or without LPS (100 ng/mL, 6 h) treatment. (*B*) qRT–PCR analysis of the mRNA levels of *Il12a*, *Il12b*, and *Il23a* in WT and *Trim14*$^{-/-}$ BMDCs treated with LPS at the indicated time points. (*C–G*) WT and *Trim14*$^{-/-}$ mice (n = 5 per group) were immunized with MOG(35–55) and PTX to induce EAE. WT and *Trim14*$^{-/-}$ mice were scored daily for disease severity (*C*). At 14 d posttreatment, brain tissues of these mice were collected, stained with H&E and assayed by a light microscope at 20× magnification. (Scale bar, 100 μm.) Red arrows show the infiltration of immune cells (*D*). At 14 d posttreatment, the brains and spinal cords of these mice were collected to detect the infiltration of IL-17A$^+$CD4$^+$ cells and IL-21$^+$CD4$^+$ cells into the CNS (brain and spinal cord) by flow cytometry analysis (*E*). At 14 d posttreatment, cell lysates of spinal cords (*F*) and brains (*G*) of these mice were harvested to detect the mRNA levels of *Il12a*, *Il12b*, and *Il23a* by qRT–PCR analysis. In *A* and *B*, bar graphs show mean values ± SEM, and the *P* values were calculated by unpaired two-tailed Student's *t* test (three independent experiments). In *C* and *E–G*, the data are the mean values ± SD, and the *P* values were calculated by unpaired two-tailed Student's *t* test (n = 5); **P* < 0.05, ***P* < 0.01, ****P* < 0.001, *****P* < 0.0001.

USP14/*BRCC3*-DKO cells treated with TNF-α (Fig. 5*F*). The mammalian target of rapamycin (mTOR) inhibitor rapamycin (Rapa) induced autophagic degradation of KDM4D in both WT and DKO cells, which could be rescued by bafilomycin A1 (BafA1) treatment (*SI Appendix*, Fig. S5*J*). We also observed that *USP14*/*BRCC3*-DKO enhanced the K63-linked ubiquitination of KDM4D, which was not inhibited by TRIM14 (Fig. 5*G*). To further confirm the function of DUBs in KDM4D stabilization, we constructed a plasmid encoding a fusion protein of the USP domain of USP14 and TRIM14 (Myc-fUT14) and found that it stabilized KDM4D even in *USP14*/*BRCC3*-DKO HEK293T cells (*SI Appendix*, Fig. S5*K*), indicating that DUB activity is required for TRIM14-mediated KDM4D stabilization. Collectively, these results suggest that TRIM14 recruits USP14 and BRCC3 to cleave the K63-linked polyubiquitin chains of KDM4D and protected it from autophagic degradation.

TRIM14-Deficient Mice Are Resistant to Inflammation. KDM4D was reported to specifically demethylate H3K9me3 to regulate the transcription of the proinflammatory cytokines *Il12* and *Il23*, which enhanced autoimmune inflammation in an EAE model (20). We found that LPS promoted the removal of H3K9me3 at the *Il12b* promoter in WT BMDCs via chromatin IP (ChIP) assays (Fig. 6*A*). Compared with WT BMDCs, *Trim14*$^{-/-}$ BMDCs showed higher levels of H3K9me3 at the promoters *Il12b*, *Il12a*, and *Il23a*, especially after LPS treatment (Fig. 6*A* and *SI Appendix*, Fig. S6*A*). Consistent results were observed in WT and *TRIM14*-KO HeLa cells (*SI Appendix*, Fig. S6*B*). We next investigated whether TRIM14 promoted *Il12* and *Il23* expression. The mRNA levels of *Il12a*, *Il12b*, and *Il23a* in *Trim14*$^{-/-}$ BMDCs were significantly decreased compared with those in WT BMDCs treated with LPS (Fig. 6*B*). To identify the gene occupancies at the genomic level, we performed a ChIP-sequencing (ChIP-seq) assay of H3K9me3 in WT and *Trim14*$^{-/-}$ BMDCs that were subsequently treated with LPS. *Trim14* deficiency changed the distribution pattern of H3K9me3 at the genomic level (*SI Appendix*, Fig. S6 *C* and *D*), and the occupied genes mainly contributed to the MAPK signaling pathway (*SI Appendix*, Fig. S6*E*). After LPS stimulation, the occupied genes were mainly involved with

the T helper (Th) cell differentiation pathway compared to those in untreated cells (*SI Appendix*, Fig. S6*E*). Consistent with these findings, the occupancy profile of H3K9me3 was increased at the *Il23a* and *Il17b* loci in *Trim14*$^{-/-}$ BMDCs treated with LPS compared with that in WT BMDCs; the occupancy profile of H3K9me3 at the *Il13* and *Il6* loci in *Trim14*$^{-/-}$ BMDCs treated with LPS were similar to that in WT BMDCs (*SI Appendix*, Fig. S6*F*).

These results further support the hypothesis that TRIM14 modulates the differentiation of Th cells to promote an inflammatory response. By comparing the phenotypes of WT and *Trim14*$^{-/-}$ EAE mouse models immunized with the myelin oligodendrocyte glycoprotein (MOG) peptide MOG(35–55) and pertussis toxin (PTX), we found that the *Trim14*$^{-/-}$ mice exhibited reduced clinical symptom severity of EAE (Fig. 6*C*), with less infiltration of immune cells into the brain (Fig. 6*D*). Immunofluorescence staining showed a decreased infiltration of CD45^{+} immune cells into the brains of *Trim14*$^{-/-}$ mice compared with WT mice (*SI Appendix*, Fig. S7*A*). Similarly, flow cytometry analysis indicated reduced quantities of IL17A^{+}CD4^{+} cells (Q2) and IL21^{+}CD4^{+} cells (Q6) in the CNS (brain and spinal cord) of *Trim14*$^{-/-}$ mice relative to WT mice (Fig. 6*E* and *SI Appendix*, Fig. S7*B*). The mRNA levels of *Il12a*, *Il12b*, and *Il23a* were decreased in both the spinal cord (Fig. 6*F*) and brain (Fig. 6*G*). In summary, our data illustrate that TRIM14 deficiency helps resolve inflammation to promote resistance to EAE.

Discussion

Accumulating evidence has shown that histone modifications, especially histone methylation, play a critical role in controlling the expression of specific inflammatory cytokines at the epigenetic level. In this study, we identified TRIM14 as a positive regulator of *Il12b* and *Il23a* expression as it maintains KDM4D stability. TRIM14 deficiency down-regulated KDM4D protein levels to suppress LPS- or TNF-α–induced transcription of *Il12* and *Il23* by enhancing H3K9me3 at their promoters in DCs. IL-12 and IL-23 are important in the polarization of CD4^{+} T cells to Th1 and Th17 cells and thereby affect the development of EAE (26). It has been reported that deficiency of Trabid, a DUB known to prevent proteasomal degradation of KDM4D, inhibits the infiltration of immune cells into the CNS in an EAE model (20). Here, we found that TRIM14 prevented autophagic degradation of KDM4D, which was another way of stabilizing the KDM4D protein. Consistent with these findings, we found that TRIM14-deficient mice had lower infiltration of IL-17A^{+}CD4^{+} T cells and IL-21^{+}CD4^{+} T cells into the CNS and that these mice were more resistant to CNS inflammation.

Autophagy is induced by nutrient starvation or stress and involves the formation of autophagosomes for the degradation and recycling of intracellular organelles and proteins (23). Macroautophagy can be in bulk or selective according to the cargo sequestered (27). During EBSS-induced autophagy, most organelles and proteins are sequestered into autophagosomes for degradation, which is nonselective. However, the cargo receptor OPTN specifically recognizes KDM4D as a substrate and delivers it to autophagosomes for selective autophagic degradation. Upon LPS treatment, the TRIM14 protein level is up-regulated to inhibit the interaction of KDM4D and OPTN, causing an accumulation of KDM4D.

Autophagy is an important cellular process that mainly occurs in the cytoplasm. Nuclear components are translocated to the cytoplasm for autophagic degradation. p62 is a nuclear cargo receptor that has been reported to interact with nuclear RNF168, an E3 ligase, to impair histone ubiquitination and DNA damage repair (28). OPTN is mainly located in the cytoplasm of neurons in healthy donors, yet colocalized OPTN-ubiquitin-p62 complex puncta have been observed in intranuclear inclusions of neuronal intranuclear inclusion disease patients (29, 30). In this study, we found that OPTN was mainly located in the cytoplasm, yet we observed the colocalization of KDM4D and TRIM14 in both the nucleus and cytoplasm. The possibility that TRIM14 functions as a coreceptor that mediates the shuttling of nuclear cargo merits further study.

Numerous studies have shown that polyubiquitin chains are recognition signals for cargo receptors (23). Unlike the proteasomal pathway, where K48-linked ubiquitin chains serve as a major degradation signal, we and other groups have shown that polyubiquitin chains of other lineages can also be recognized by cargo receptors for autophagic degradation (9, 11, 31–33). K63-linked ubiquitination was originally reported as a nondegradation signal that mediated the activation of signaling cascades in innate immunity (34, 35). We recently found that K63-linked polyubiquitin chains on p100/p52 were recognized by p62 and served as a degradation signal to restrict inflammation (10). Here, we found that OPTN can also bind to the K63-linked ubiquitin chains of KDM4D to mediate its degradation. In addition, TRIM14 cooperated with USP14 and BRCC3 to cleave the K63-linked ubiquitin chains of KDM4D and prevent autophagic degradation of KDM4D. We also observed that K27-linked ubiquitination of KDM4D decreased slightly with TRIM14 overexpression (*SI Appendix*, Fig. S5*A*). Since USP14 does not specifically cleave K63-linked ubiquitin chains (36), we think the slight effect of TRIM14 on K27-linked ubiquitination may be due to the nonselective deubiquitination activity of DUBs interacting with TRIM14.

In our previous study, we found that USP14 and TRIM14 often form a deubiquitination complex to inhibit selective autophagy (9). Here, we found that BRCC3 and USP14 play redundant roles in removing the ubiquitin chains of KDM4D. Our data illustrate that TRIM14 serves as a platform to recruit USP14 and BRCC3 to deubiquitinate ubiquitin chains conjugated to KDM4D, which in turn inhibits OPTN-mediated autophagic degradation of KDM4D and up-regulates the expression of *Il12* and *Il23* by reducing H3K9me3 at their promoters to promote inflammation. However, it is an open question how KDM4D is ubiquitinated. There are three main types of E3 ligases based on their functional domains and mechanisms: RING E3s, HECT E3s, and RBR E3s (8). The largest family of ubiquitin ligases, RING E3s, include a zinc-binding domain called RING (Really Interesting New Gene). Many members of the TRIM superfamily contain a RING domain and can thus function as E3 ligases (37). TRIM14 does not contain a RING domain. We hypothesize that TRIM proteins potentially function as E3 ligases of KDM4D, although this has not yet been reported. Interestingly, we found that several E3 ligases of the TRIM family interacted with KDM4D in our MS dataset: TRIM4, TRIM8, TRIM9, TRIM11, TRIM23, TRIM32, TRIM36, TRIM37, TRIM50, TRIM52, TRIM62, TRIM68, and TRIM71. Whether these TRIMs are in charge of KDM4D ubiquitination needs further investigation.

Collectively, our data provide evidence for the autophagic control of epigenetic regulation in inflammation, as the TRIM14–USP14–BRCC3 complex stabilizes KDM4D and prevents its autophagic degradation in DCs to mediate the pathogenesis of EAE (*SI Appendix*, Fig. S8). These results suggest TRIM14 is a potential target for therapy for inflammation-related diseases in the future.

Materials and Methods

Generation of *Trim14*$^{-/-}$ Mice. *Trim14*$^{-/-}$ mice were created with a CRISPR/Cas9 system, which was described in a previous study (9). The mice were raised in a specific-pathogen free animal facility at Sun Yat-sen University. All the experimental protocols related to the handling of mice were approved by the institution's Animal Care and Use Committee.

Induction of EAE Model. Six-week-old female mice were immunized with MOG(35–55) (2 mg/mL, diluted with PBS) equally mixed with CFA (4 mg/mL, completed with inactivated *Mycobacterium tuberculosis*) for a total of 400 μL per mouse. Two solutions were mixed on ice by ultrasound for 5 min to form emulsions, and then frozen at −80 °C. The emulsion was slowly thawed at 4 °C. These mix–freeze–thaw steps were repeated two times. The emulsion was filtered and injected into the portion of the extremities closest to the lymph node to induce T cell-dependent inflammation. PTX (200 μL, 2 mg/mL) was intraperitoneally injected on day 0 and day 2. The health of the mice was observed, and the daily clinical score was recorded using the standard scale: 0) no clinical sings; 1) weak tail; 2) paraparesis (weakness, partial paralysis of one or two hind legs); 3) paraplegia (complete paralysis of two hind legs); 4) paraplegia with weakness or paralysis of forelimb; and 5) moribund or death. Jelly was provided on the cage floor in addition to food and water.

Flow Cytometry Analysis. Single-cell suspensions of brains and spinal cords isolated from WT and *Trim14*$^{-/-}$ EAE mouse models were washed in PBS with 10% FBS. Cells were stained with the following fluorescence-labeled antibodies: APC-Cy7–conjugated anti-CD45 (BD, B557659), PE-ef610–conjugated CD4 (eBioscience, 61004382), BV785-conjugated anti-CD8 (eBioscience, 60-5961), BV510-conjugated anti–IL-17A (BD, 563295) and PE-conjugated anti–IL-21 (R&D, IC594P-100). Subsequently, cell suspensions were subjected to flow cytometry for analysis. Statistical analysis was performed by Flowjo_v10.

Fluorescence Microscopy. Cells were cultured on glass-bottomed culture dishes (Nest Scientific) and washed with PBS three times before collection. Then, the cells were fixed with 4% paraformaldehyde for 15 min and washed with PBS. Subsequently, methyl alcohol was added for 30 min at –20 °C to permeabilize the cells. After the cells were washed with PBS three times for 5 min, they were blocked with PBS supplemented with 6% fetal goat serum for 1 h and incubated with primary antibodies diluted in PBS supplemented with 6% fetal goat serum overnight at 4 °C. The cells were washed three times and stained with the indicated fluorescently labeled secondary antibody on the second day. DAPI staining was done last. Confocal images were captured by a microscope (LSM710; Carl Zeiss). The images were analyzed in ImageJ software (NIH). Approximately 50 cells were quantified per group.

Isolation of BMDCs. BM cells were isolated from WT or *Trim14*$^{-/-}$ mice. Then, they were cultured in RPMI medium 1640 containing 10% FBS. We added GM-CSF (20 ng/mL) and IL-4 (10 ng/mL) for 7 d to induce BMDCs. Half of the culture medium was changed after three days and GM-CSF and IL-4 were supplemented.

Co-IP and Immunoblotting Analysis. For co-IP of KDM4D and OPTN or LC3, samples were treated with EBSS to induce autophagosome formation, since the interaction of KDM4D and OPTN or LC3 increased when global autophagy was initiated. BafA1 is an H^+-ATPase inhibitor that blocks autophagosome degradation in autolysosomes (38); therefore, the interaction between these proteins is detected more easily in the presence of BafA1. Then, the cells were lysed in low salt lysis buffer (LSB, 50 mM Hepes [Invitrogen, 15630-080], 10% glycerol [Vetec, V900122-6X500ML], 1% Triton X-100 [Sigma, T9284-500ML], 150 mM NaCl [Guangzhou Chemical Reagent Factory, 7647-14-5], 1 mM EDTA [Vetec, V900106-500G], 1.5 mM $MgCl_2$ [Vetec, V900020-6X500G], supplemented with protease inhibitor and phosphorylation inhibitor) on ice for 30 min. The extracts were centrifuged for 5 min at 4 °C. For co-IP, the supernatants were incubated with the indicated antibody overnight at 4 °C, followed by the addition of Protein A/G beads (Pierce). For the ubiquitination assay of KDM4D, 1% SDS was added to the lysis buffer, and extracts were boiled for 10 min to denature the sample. Then, the samples were diluted to 0.2% SDS for IP. For IP with anti-Flag, anti-Flag beads (Sigma) were used. The beads were washed several times by full immersion in LSB and eluted with 2× SDS loading buffer for subsequent SDS/PAGE. For immunoblotting analysis, the supernatants were mixed with 5× SDS loading buffer for SDS/PAGE. The proteins were transferred to PVDF membranes (Bio-Rad) for further antibody detection. Image Lab 5.2.1 (Bio-Rad) software was used to capture the immunoblot signal and to examine all the immunoblots to avoid overexposured images. Short-term exposure images in the linear range were chosen for protein quantification by ImageJ software (NIH).

Cell Culture. HEK 293T and HeLa cells were cultured in DMEM (HyClone) with 10% FBS (GenStar) and 1% L-glutamine (Gibco). BMDCs were cultured in RPMI-1640 medium (Gibco) with 10% FBS (GenStar) and 1% L-glutamine (Gibco). Cells were incubated at 37 °C in 5% CO_2.

Plasmids and Small Interfering RNA Transfection. TRIM14, KDM4D, OPTN, and the other plasmids mentioned were cloned into the pcDNA3.1 vector for transient expression. TRIM14 was cloned into FG-EH-DEST for retroviral expression. Point mutations, including Flag-KDM4D (K4459R) and Flag-KDM4D (K472R), were generated by site-directed mutagenesis (Sbsgene). For the HA-tagged specific ubiquitin chain (K6, K11, K27, K29, K33, K48, and K63) plasmids, all the other K residues were substituted with R on ubiquitin but the indicated K; thus, such ubiquitin mutants could only form polyubiquitin chains by conjugation at the indicated K site. *TRIM14* small interfering RNA (siRNA) and control (scramble) siRNA were obtained from Vigene. For transfection, plasmids were mixed with the transfection reagent (GenStar) at an optimum ratio of 1:3. After vortexing and short centrifugation, the mix was allowed to stand for 10 min before being added to the cell culture. For transfection of siRNA, siRNA was mixed with Lipofectamine RNAi MAX (Invitrogen) at an optimum ratio of 1:1. After vortexing and short centrifugation, the mix was allowed to stand for 15 min before being added to the cell culture. The RNA oligonucleotides used in this study were:

human *TRIM14*-siRNA #1 forward: CCGAGAAGCUCAAGGCUAA
reverse: UUAGCCUUGAGCUUCUCGG
human *TRIM14*-siRNA #2 forward: CAGAUUACUACUUGACGAA
reverse: UUCGUCAAGUAGUAAUCUG
human *TRIM14*-siRNA #3 forward: CGUGCAGAAACUCAGCCAA
reverse: UUGGCUGAGUUUCUGCACG
human *TRIM14*-siRNA #4 forward: CCAAGAAAUUCAUUGAUAA
reverse: UUAUCAAUGAAUUUCUUGG
human *UBE2N*-siRNA #1 forward: GGCUAUAUGCCAUGAAUAAUU
reverse: AAUUAUUCAUGGCAUAUAGCC
human *UBE2N*-siRNA #2 forward: CCAGAUGAUCCAUUAGCAAUU
reverse: AAUUGCUAAUGGAUCAUCUGG

Reagents. We used StarFect High-efficiency Transfection Reagent (GenStar) to transfect plasmids into cells according to the manufacturer's instructions. Cells were incubated in EBSS (Gibco) to induce autophagy. Puromycin (P9620), MG132 (C-2211-5MG), doxycycline (Doxy; D9891), BafA1 (H2714), 3-MA (M9281-100MG), LPS (L4391-1MG), cycloheximide from microbes (CHX, C1988-1 g), and Triton X-100 (T9284-500ML) were purchased from Sigma. Recombinant TNF-α (300-01A) was purchased from PeproTech. IOX1 (HY-12304) was purchased from MCE. LSB (50 mM Hepes, 150 mM NaCl, 1 mM EDTA, 10% glycerol, 1.5 mM $MgCl_2$, and 1% Triton X-100) was used. Hepes (15630-080) was purchased from Invitrogen. NaCl (7647-14-5) was purchased from Guangzhou Chemical Reagent Factory. EDTA (V900106-500G), glycerol (V900122-6X500ML) and $MgCl_2$ (V900020-6X500G) were purchased from Vetec. MOG(35–55) (T510219-0005) was purchased from Sangon Biotech. CFA (F5881) was purchased from Sigma. PTX (#180) was purchased from ListLabs.

Antibodies. Anti-TRIM14 (sc-79761), anti-ubiquitin (sc-8017), goat anti-mouse IgG-HRP, and goat anti-rabbit IgG-HRP were purchased from Santa Cruz. Anti-K63-linkage polyubiquitin (D7A11) was purchased from Cell Signaling Technology. Anti-H3K4me3 (A2357) was purchased from Abclonal. Anti-H3K9me3 (61013) and anti-H3K9me2 (39375) were purchased from Active Motif. Anti-Histone H3 antibody (ab1791) was purchased from Abcam. Anti-H2B (12364S), anti-H2A (12349S), anti-BRCC3 (#18215), and anti-UBE2N (#6999S) were purchased from CST. Horseradish peroxidase (HRP) anti-Flag (A8592) and anti-USP14 (WH0009097M4-100UG) were purchased from Sigma. Anti-KDM4D (ab93694) was purchased from Abcam. HRP-anti-HA (12013819001) was purchased from Roche. Anti-c-Myc-HRP (11814150001) was purchased from Roche Applied Science. Anti-ATG5 (12994S) was purchased from Cell Signaling Technology. Anti-NDP52 (12229-1-AP) and anti-OPTN (10837-1-AP) were purchased from Proteintech.

RNA Extraction and qRT-PCR. Total RNA was isolated by TRIzol Reagent (Invitrogen) and reverse transcribed to cDNA by reverse transcriptase (Takara). We applied SYBR Green qPCR Mix (GenStar) for real-time PCR and normalized the data to GAPDH. The following primers were used:

Il12a forward primer: 5′-ACTAGAGAGACTTCTTCCACAACAAGAG-3′
Il12a reverse primer: 5′-GCACAGGGTCATCATCAAAGAC-3′
Il12b forward primer: 5′-GGAGACACCAGCAAAACGAT-3′
Il12b reverse primer: 5′-TCCAGATTCAGACTCCAGGG-3′
Il23a forward primer: 5′-GCCAAGAAGACCATTCCCGA-3′
Il23a reverse primer: 5′ TCAGTGCTACAATCTTCTTCAGAGGACA3′
mGapdh forward primer: 5′GAAGGGCTCATGACCACAGT-3′
mGapdh reverse primer:5′-GGATGCAGGGATGATGTTCT-3′

ChIP Assays. ChIP assays were performed with BMDCs (1×10^8) stimulated with LPS (100 ng/mL) for 6 h and then fixed for the experiments as described

by the manufacturers of the SimpleChIP Enzymatic Chromatin IP Kit (#9003, Cell Signaling). Then, qPCR was performed to quantify precipitated DNA by using the following primer pairs:

Il12a forward primer: 5′-ACGCACTTGTCCTTGAGATG-3′
Il12a reverse primer: 5′-CTGACCTTGGGAGACACATTT-3′
Il12b forward primer: 5′-CATTTCCTCTTAACCTGGGATTTC-3′
Il12b reverse primer: 5′-CTGCTCCTGGTGCTTATATACT-3′
Il23a forward primer: 5′-AGGCACTAGGAAAGAGGATCTA-3′
Il23a reverse primer: 5′-GTTCATACCTGGAGGAGTTGG-3′

ChIP-Seq Analysis. For ChIP-seq analysis, paired-end sequencing reads from ChIP-seq were mapped to mm10 mouse reference genome by using Bowtie2 (v2.2.5) with default parameters, and the SAM files were converted to BAM files. The unmapped and multimapped reads were discarded. Then PCR duplicates were marked by Picard Tools (v 2.14.0). ChIP-seq peaks were called by MACS2 (v 2.2.6) with default options. The Bowtie-aligned peaks were visualized by using Integrated Genome Browser (39). Peaks were annotated to the gene with the closest transcription start sites by ChIPseeker (v1.28.3) available on Bioconductor. Enrichment analysis was performed by clusterProfiler (v4.0.5).

Statistical Analysis. Statistical analysis was conducted in Prism software. Two-tailed unpaired *t* tests were used to detect significant differences. ns, not significant, $*P < 0.05$, $**P < 0.01$, $***P < 0.001$, $****P < 0.0001$.

Data Availability. ChIP-seq data were deposited in the Sequence Read Archive repository under the accession code PRJNA800612. All other study data are included in the main text and *SI Appendix*.

ACKNOWLEDGMENTS. This work was supported by the National Key R&D Program of China under Grant 2020YFA0908700, the National Natural Science Foundation of China (92042303, 31870862), and the Guangdong Basic and Applied Basic Research Foundation (2020B1515120090).

1. A. J. Clarke, A. K. Simon, Autophagy in the renewal, differentiation and homeostasis of immune cells. *Nat. Rev. Immunol.* **19**, 170–183 (2019).
2. V. Deretic, T. Saitoh, S. Akira, Autophagy in infection, inflammation and immunity. *Nat. Rev. Immunol.* **13**, 722–737 (2013).
3. B. Levine, N. Mizushima, H. W. Virgin, Autophagy in immunity and inflammation. *Nature* **469**, 323–335 (2011).
4. K. Yamamoto *et al.*, Autophagy promotes immune evasion of pancreatic cancer by degrading MHC-I. *Nature* **581**, 100–105 (2020).
5. D. Mijaljica *et al.*, Receptor protein complexes are in control of autophagy. *Autophagy* **8**, 1701–1705 (2012).
6. T. Johansen, T. Lamark, Selective autophagy: ATG8 family proteins, LIR motifs and cargo receptors. *J. Mol. Biol.* **432**, 80–103 (2020).
7. J. Liu *et al.*, Targeting the ubiquitination/deubiquitination process to regulate immune checkpoint pathways. *Signal Transduct. Target. Ther.* **6**, 28 (2021).
8. M. Di Rienzo, A. Romagnoli, M. Antonioli, M. Piacentini, G. M. Fimia, TRIM proteins in autophagy: Selective sensors in cell damage and innate immune responses. *Cell Death Differ.* **27**, 887–902 (2020).
9. M. Chen *et al.*, TRIM14 inhibits cGAS degradation mediated by selective autophagy receptor p62 to promote innate immune responses. *Mol. Cell* **64**, 105–119 (2016).
10. M. Chen *et al.*, TRIM14 promotes noncanonical NF-κB activation by modulating p100/p52 stability via selective autophagy. *Adv. Sci. (Weinh.)* **7**, 1901261 (2019).
11. Z. Zhao *et al.*, USP38 couples histone ubiquitination and methylation via KDM5B to resolve inflammation. *Adv. Sci. (Weinh.)* **7**, 2002680 (2020).
12. S. Zhao *et al.*, H3K4 methylation regulates LPS-induced proinflammatory cytokine expression and release in macrophages. *Shock* **51**, 401–406 (2019).
13. W. Yu *et al.*, One-carbon metabolism supports S-adenosylmethionine and histone methylation to drive inflammatory macrophages. *Mol. Cell* **75**, 1147–1160.e5 (2019).
14. M. Francis *et al.*, Histone methylation mechanisms modulate the inflammatory response of periodontal ligament progenitors. *Stem Cells Dev.* **28**, 1015–1025 (2019).
15. S. Chang, T. M. Aune, Dynamic changes in histone-methylation 'marks' across the locus encoding interferon-γ during the differentiation of T helper type 2 cells. *Nat. Immunol.* **8**, 723–731 (2007).
16. L. Austenaa *et al.*, The histone methyltransferase Wbp7 controls macrophage function through GPI glycolipid anchor synthesis. *Immunity* **36**, 572–585 (2012).
17. D. Zhao *et al.*, H3K4me3 demethylase Kdm5a is required for NK cell activation by associating with p50 to suppress SOCS1. *Cell Rep.* **15**, 288–299 (2016).
18. T. C. Fang *et al.*, Histone H3 lysine 9 di-methylation as an epigenetic signature of the interferon response. *J. Exp. Med.* **209**, 661–669 (2012).
19. Y. Zhu, D. van Essen, S. Saccani, Cell-type-specific control of enhancer activity by H3K9 trimethylation. *Mol. Cell* **46**, 408–423 (2012).
20. J. Jin *et al.*, Epigenetic regulation of the expression of Il12 and Il23 and autoimmune inflammation by the deubiquitinase Trabid. *Nat. Immunol.* **17**, 259–268 (2016).
21. I. Tanida, T. Ueno, E. Kominami, LC3 and autophagy. *Methods Mol. Biol.* **445**, 77–88 (2008).
22. K. M. J. Sparrer *et al.*, TRIM23 mediates virus-induced autophagy via activation of TBK1. *Nat. Microbiol.* **2**, 1543–1557 (2017).
23. C. Kraft, M. Peter, K. Hofmann, Selective autophagy: Ubiquitin-mediated recognition and beyond. *Nat. Cell Biol.* **12**, 836–841 (2010).
24. H. Yan *et al.*, Inhibition of UBE2N-dependent CDK6 protein degradation by miR-934 promotes human bladder cancer cell growth. *FASEB J.* **33**, 12112–12123 (2019).
25. A. Dikshit *et al.*, UBE2N promotes melanoma growth via MEK/FRA1/SOX10 signaling. *Cancer Res.* **78**, 6462–6472 (2018).
26. M. A. Kroenke, T. J. Carlson, A. V. Andjelkovic, B. M. Segal, IL-12- and IL-23-modulated T cells induce distinct types of EAE based on histology, CNS chemokine profile, and response to cytokine inhibition. *J. Exp. Med.* **205**, 1535–1541 (2008).
27. S. Kaushik, A. M. Cuervo, The coming of age of chaperone-mediated autophagy. *Nat. Rev. Mol. Cell Biol.* **19**, 365–381 (2018).
28. Y. Wang *et al.*, Autophagy regulates chromatin ubiquitination in DNA damage response through elimination of SQSTM1/p62. *Mol. Cell* **63**, 34–48 (2016).
29. M. Nakamura, M. E. Murray, W.-L. Lin, H. Kusaka, D. W. Dickson, Optineurin immunoreactivity in neuronal and glial intranuclear inclusions in adult-onset neuronal intranuclear inclusion disease. *Am. J. Neurodegener. Dis.* **3**, 93–102 (2014).
30. C. Cupidi *et al.*, Refining the spectrum of neuronal intranuclear inclusion disease: A case report. *J. Neuropathol. Exp. Neurol.* **78**, 665–670 (2019).
31. S. Geisler *et al.*, PINK1/Parkin-mediated mitophagy is dependent on VDAC1 and p62/SQSTM1. *Nat. Cell Biol.* **12**, 119–131 (2010).
32. Z. Zhou *et al.*, K63 ubiquitin chains target NLRP3 inflammasome for autophagic degradation in ox-LDL-stimulated THP-1 macrophages. *Aging (Albany NY)* **12**, 1747–1759 (2020).
33. A. Chargui *et al.*, The carcinogen cadmium activates lysine 63 (K63)-linked ubiquitin-dependent signaling and inhibits selective autophagy. *Cancers (Basel)* **13**, 2490 (2021).
34. C. H. Emmerich *et al.*, Activation of the canonical IKK complex by K63/M1-linked hybrid ubiquitin chains. *Proc. Natl. Acad. Sci. U.S.A.* **110**, 15247–15252 (2013).
35. F. Ohtake, Y. Saeki, S. Ishido, J. Kanno, K. Tanaka, The K48-K63 branched ubiquitin chain regulates NF-κB signaling. *Mol. Cell* **64**, 251–266 (2016).
36. D. Flierman *et al.*, Non-hydrolyzable diubiquitin probes reveal linkage-specific reactivity of deubiquitylating enzymes mediated by S2 pockets. *Cell Chem. Biol.* **23**, 472–482 (2016).
37. K. Ozato, D.-M. Shin, T.-H. Chang, H. C. Morse, 3rd, TRIM family proteins and their emerging roles in innate immunity. *Nat. Rev. Immunol.* **8**, 849–860 (2008).
38. S. Jin *et al.*, m^6A RNA modification controls autophagy through upregulating ULK1 protein abundance. *Cell Res.* **28**, 955–957 (2018).
39. N. H. Freese, D. C. Norris, A. E. Loraine, Integrated genome browser: Visual analytics platform for genomics. *Bioinformatics* **32**, 2089–2095 (2016).